GEOCHEMISTRY

Recycled selenium in hot spot–influenced lavas records ocean-atmosphere oxygenation

Aierken Yierpan[1]*, Stephan König[1]*, Jabrane Labidi[1,2], Ronny Schoenberg[1,3]

Oxygenation of Earth's oceans and atmosphere through time has consequences for subducted surface signatures that are now stored in the mantle. Here, we report significant mass-dependent selenium isotope variations in modern hot spot–influenced oceanic lavas. These variations are correlated with tracers of mantle source enrichment, which can only be explained by incorporation of abyssal pelagic sediments subducted from a redox-stratified mid-Proterozoic ocean. Selenium geochemical signatures of these sediments have mostly been preserved during long-term recycling and may therefore complement the global surface sediment record as ancient oxygen archives. Combined deep mantle and surface perspectives, together with emerging models for atmospheric oxygen based on selenium systematics, further imply a significantly oxygenated ocean-atmosphere system throughout the mid-Proterozoic.

INTRODUCTION

Earth's surface oxygenation and mantle evolution are intimately linked by plate tectonics (*1*–*5*). Constraints on ocean-atmosphere redox evolution through time are typically obtained from the geochemical signals archived in the surface sedimentary record (*6*–*11*). However, most of deep-ocean sediments such as those deposited beyond the continental slopes were likely obliterated from the geological record because of subduction recycling of the oceanic crust (*11*, *12*). Earth's interior therefore provides complementary clues to secular changes in the surface redox conditions, which impart unique geochemical signatures into the mantle via subduction (*13*–*17*). Here, we use selenium (Se) isotopic variations in hot spot–influenced oceanic lavas to infer the recycled Se isotopic and elemental composition of mid-Proterozoic subducted sediments and pyrites. Selenium is a chalcophile redox-sensitive element and exhibits a variety of oxidation states (−2, 0, +4, and +6) in different geological reservoirs (section S1) (*18*). Because of the distinct mobility and large isotopic fractionation between different Se species in low-temperature environments, Se isotopic and elemental abundances of marine sediments and sedimentary pyrites have emerged as new redox proxies in the ocean-atmosphere system (section S1 and fig. S1) (*7*, *18*–*20*). Global marine sediments display large Se isotopic variations, with δ^{82}Se values (deviation in ^{82}Se/^{76}Se relative to the standard) between ~−3 per mil (‰) and +3‰ (Fig. 1A). There is a marked shift in sediment average δ^{82}Se toward lighter values from the Precambrian to Phanerozoic (from ~+0.54‰ to −0.17‰), reflecting Late Neoproterozoic deep-ocean oxygenation (*20*) (Fig. 1A). By contrast, δ^{82}Se variability in mantle samples is rather limited yet still resolvable (~−0.3‰ to +0.3‰; Fig. 1, A and B). Selenium isotope signatures of mantle reservoirs should be highly sensitive to the presence of recycled sediments, given the large difference in Se contents between the igneous and surface reservoirs (~1 to 2 orders of magnitude difference; Fig. 1A) and the absence of isotope fractionation during high-temperature mantle processes involving Se partitioning between sulfides and silicate melt (section S2) (*21*). Selenium systematics are thus particularly sensitive

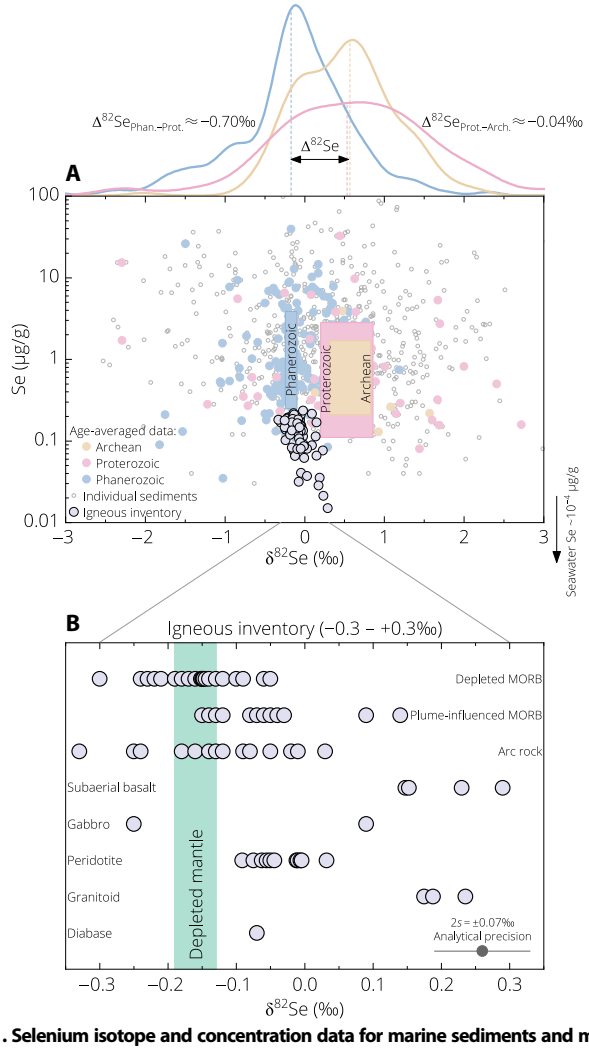

Fig. 1. Selenium isotope and concentration data for marine sediments and mantle samples. (**A**) Colored boxes show the mean δ^{82}Se [± 95% confidence interval (CI)] and Se contents (log-normal mean ± 1*s*) of sediments (N = 759) sorted by age intervals. The group means are calculated over sediment data averaged by depositional age (color-coded filled circles). Top: Gaussian kernel density estimations of sediment δ^{82}Se for each age interval and average isotopic shift (dashed lines). (**B**) Igneous inventory (N = 87). The shaded field represents the depleted mantle estimate (Table 1). See section S1 for related references.

[1]Isotope Geochemistry, Department of Geosciences, University of Tübingen, 72076 Tübingen, Germany. [2]Institut de Physique du Globe de Paris, 1 rue Jussieu, 75005 Paris, France. [3]Department of Geology, University of Johannesburg, 2092 Johannesburg, South Africa.
*Corresponding author. Email: aierken.yierpan@uni-tuebingen.de (A.Y.); skonig@gmx.de (S.K.)

Table 1. Selenium, sulfur, and radiogenic isotope compositions of the MAR glasses. Uncertainties on the sample δ^{82}Se are 95% CI if the number of analyses $n_i > 3$, or the $2s_p$ external reproducibility of 0.08‰ (estimated for glass matrices) if $n_i \leq 3$. n = number of sample digestions (number in parentheses refers to n_i). See the Supplementary Materials and Methods for the sample literature data.

Sample	Type	δ^{82}Se (‰)	n	δ^{34}S (‰)	^{87}Sr/^{86}Sr	^{143}Nd/^{144}Nd
S-MAR						
EW9309 41D-1g	Depleted MORB	−0.06 ± 0.08	2	−1.04	0.703273	0.513048
EW9309 40D-1g		−0.18 ± 0.08	2 (3)	−1.21	0.702997	0.513033
EW9309 34D-1g	Discovery anomaly	−0.07 ± 0.08	1	−1.23	0.703544	0.512868
EW9309 33D 1g		−0.03 ± 0.08	2	−0.58	0.704475	0.512726
EW9309 28D-1g		−0.14 ± 0.08	2	−0.83	0.703028	0.513077
EW9309 25D-1g		+0.09 ± 0.08	4	+1.05	0.705728	0.512430
EW9309 2D-1g		−0.08 ± 0.04	3 (4)	−0.14	0.704127	0.512652
EW9309 4D-3g		−0.04 ± 0.08	2	−0.62	0.703762	0.512732
EW9309 5D 5g		−0.06 ± 0.08	2	−0.42	0.703976	0.512594
EW9309 7D-1g	LOMU anomaly	+0.14 ± 0.08	3	+0.03	0.705093	0.512489
EW9309 8D-1g		−0.05 ± 0.08	3	−0.48	0.704286	0.512752
EW9309 9D-3g		−0.03 ± 0.04	6	−0.50	0.704284	0.512873
EW9309 15D-1g	Shona anomaly	−0.13 ± 0.08	2	−1.38	0.702741	0.513008
EW9309 21D-1g		−0.12 ± 0.08	2	−1.06	0.703115	0.512818
EW9309 23D-1g		−0.15 ± 0.08	2	−0.91	0.703058	0.512886
EW9309 22D-3g		−0.08 ± 0.08	1 (2)	−0.59	0.703576	0.512893
N-MAR						
TR138 09D-2g	Depleted MORB	−0.17 ± 0.08	1		0.70268	0.513203
TR138 08D-1g		−0.19 ± 0.08	2		0.70251	0.513226
Pacific depleted mantle*		−0.16 ± 0.03		−1.4 ± 0.5	0.70248 ± 0.00003	0.51311 ± 0.00001
Depleted mantle†		−0.16 ± 0.03		−1.4 ± 0.5	0.70211–0.70263	0.51310–0.51328

*Average δ^{82}Se (±95% CI, N = 27) and Sr-Nd isotopic ratios (±95% CI, N = 66) of PAR glasses [(*21*, *46*) and references therein]; δ^{34}S (±1*s*) from (*46*). †δ^{82}Se (±95% CI, N = 31) is estimated using all the depleted MORBs from the MAR and PAR; δ^{34}S (±1*s*) and Sr-Nd isotopic ratios from (*15*, *27*, *48*).

tracers to study ocean-atmosphere redox evolution recorded by Earth's surface and interior.

RESULTS

We measured Se isotope composition of selected mid-ocean ridge basalt (MORB) glasses from the southern and northern Mid-Atlantic Ridge (S- and N-MAR; Table 1 and fig. S2). Localized interaction between the S-MAR and Shona and Discovery hot spots resulted in prominent geochemical heterogeneities in the MORB mantle source, highlighting the presence of recycled surface materials (*15*, *22*–*24*) (Fig. 2 and fig. S3). The targeted samples cover a full spectrum of radiogenic isotope variations found in global MORB, ranging from highly depleted to enriched basalts with enriched mantle 1 (EM1), LOMU (low μ; μ = ^{238}U/^{204}Pb), and HIMU (high μ) affinities (Fig. 2; see Supplementary Materials and Methods for details). Selenium isotope compositions of the depleted MAR basalts are within error of the average Pacific-Antarctic Ridge (PAR) mantle that is devoid of any plume contribution (Table 1, Fig. 3, and fig. S4) (*21*). Together, they define a mean δ^{82}Se of −0.16 ± 0.03‰ [95% confidence interval (CI); N = 31], representing our depleted mantle estimate (section S3). Basalts exhibiting the Discovery and LOMU anomalies extend the depleted mantle range toward heavier δ^{82}Se values, with the Shona anomaly in between (Fig. 3 and section S4). There is a positive correlation between δ^{82}Se and ^{87}Sr/^{86}Sr and δ^{34}S ratios as indicators of mantle source enrichment (Fig. 3). The overall δ^{82}Se variation within the MAR suite (~0.33‰) significantly exceeds the external reproducibility of our method for MORB glasses (±0.08‰, 2 SDs or 2*s*; Materials and Methods). The calculated mean squared weighted deviation (MSWD) or reduced χ^2 for the MAR δ^{82}Se dataset is 4.71, well exceeding the 95% CI of 0.44 to 1.78 given by χ^2 statistics. This suggests that the observed dispersion in δ^{82}Se of these MORBs cannot be adequately accounted for by analytical uncertainties.

DISCUSSION

Origin of Se isotopic variability in the mantle

A χ^2 test shows that strictly depleted mantle domains have homogenous Se isotopic compositions with only subtle statistical variability (section S3). Extrapolation of the error-weighted linear regression lines (Fig. 3, A and C) to the depleted mantle average ^{87}Sr/^{86}Sr ≈ 0.70248 and δ^{34}S ≈ −1.4‰ (table S3) yields δ^{82}Se of −0.18 ± 0.03‰ and −0.15 ± 0.04‰, respectively (95% CI), which remain identical to our depleted mantle estimate.

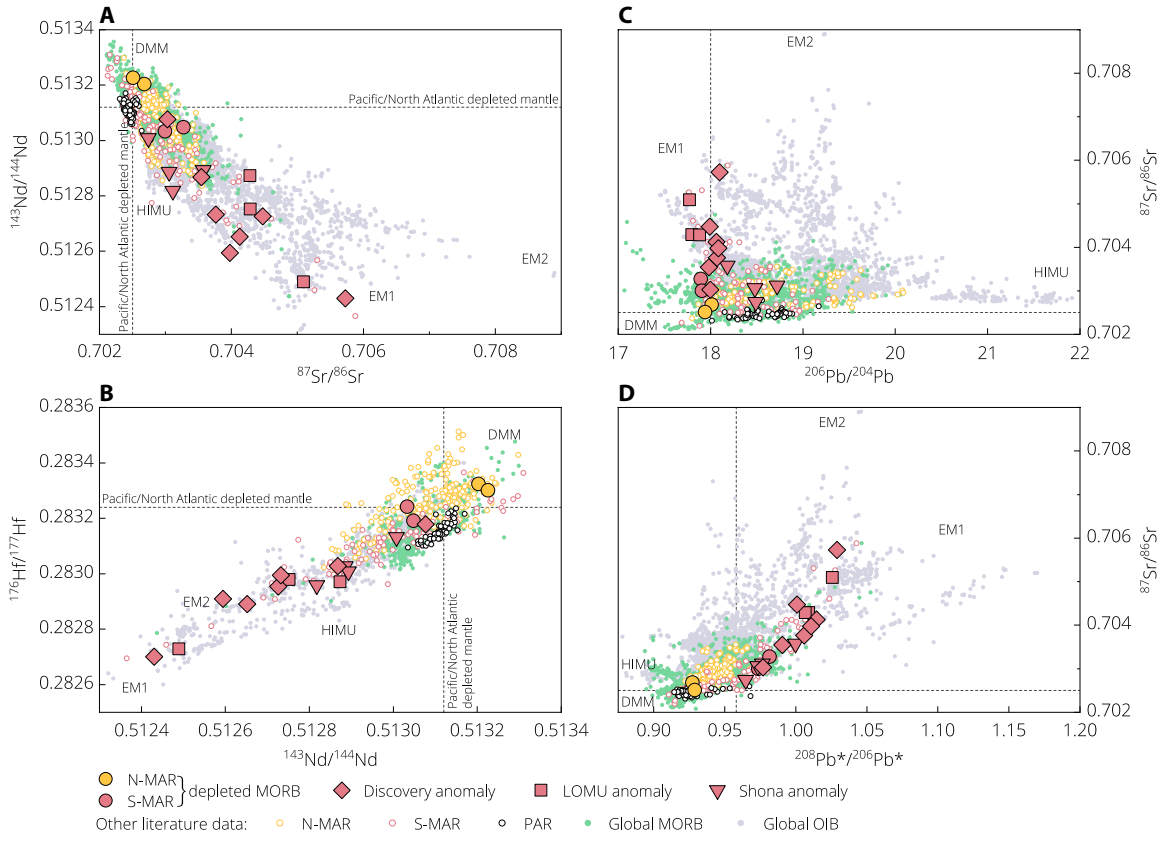

Fig. 2. Radiogenic isotope data for the studied MAR glasses. (**A** to **D**) Shown for comparison are a global compilation of MORB (*44*) and ocean island basalt (OIB; PetDB database) data and a more complete dataset for the entire MAR [S- and N-MAR basalts; precompiled by (*15*, *45*)] and PAR sample suites [(*21*, *46*) and references therein]. Solid lines denote the average composition of the Pacific and North Atlantic ambient depleted mantle (*22*). (D) $^{208}Pb^*/^{206}Pb^*$ is the time-integrated Th/U ratios [see (*44*)].

The observed correlations between $\delta^{82}Se$ and $^{87}Sr/^{86}Sr$, $^{143}Nd/^{144}Nd$, and $\delta^{34}S$ in the S-MAR basalts (Fig. 3 and fig. S5A) cannot be explained by fractionation during mantle melting and/or igneous differentiation (fig. S4 and section S2) (*21*). Instead, our data require incorporation of enriched plume components with isotopically heavier Se into the ambient asthenospheric mantle. We argue that the enrichment of heavy Se isotopes in the S-MAR can only be achieved by the addition of pelagic sediments, which were previously constrained to have a mid-Proterozoic recycling age between 1 and 2 billion years (Ga) ago based on radiogenic Pb and stable S (both mass-dependent and mass-independent) isotope systems (*15*, *22*, *23*). First, most Proterozoic sediments are enriched in ^{82}Se relative to the igneous inventory (Fig. 1A), which would readily satisfy the positive slope of the Se-Sr isotopic mixing relationship (Fig. 3A). Second, the apparent linearity of this trend requires the recycled components to have Se/Sr ratios comparable to the depleted mantle, and only pelagic sediments qualify under such criteria owing to authigenic Se enrichment (Fig. 1A). Assessment of alternative mixing models (see below) lends credence to a broadly linear mixing trend. Other recycled materials that carry EM1, LOMU, and HIMU components in the Discovery and Shona plumes [such as ancient oceanic crust, delaminated subcontinental lithospheric mantle, and lower continental crust (*22*–*24*)] have little effect on the Se isotope signature of the MAR mantle source, because either their $\delta^{82}Se$ are within the igneous inventory range (~−0.3‰ to +0.3‰; $N = 87$) or their Se contents are comparable to the MORB mantle (Fig. 1A and sections S5 and S6). This is similar to the case of S isotope systematics and highlights close geochemical relationship between Se and S during long-term crustal recycling (Fig. 3 and figs. S6 and S7), despite the large differences in the redox potential of these two systems in surface environments (section S4).

Recycled sediments from a redox-stratified ocean

Selenium isotope and elemental systematics of recycled sediments, when interpreted within the previously established framework of marine Se cycle (*7*, *18*–*20*) (section S1 and fig. S1), may reveal an average global extent of ocean oxygenation over a broad geological time interval. This is because subducted pelagic sediments give an integrated view of those continuously deposited at various depths/redox conditions in an open ocean (fig. S1) over the lifetime of subducting seafloor [e.g., ~50 to 100 million years on average (*25*) versus Se ocean residence time of 10^4 years (section S1)]. One might also expect further homogenization of Se within the subducted package during mantle storage for ~1 to 2 Ga if sedimentary sulfides (as the major host of Se) were molten at a range of convective upper mantle conditions (*21*, *26*).

The $\delta^{82}Se$-$^{87}Sr/^{86}Sr$ covariation in our MORB data (Fig. 3A)—combined with the previously established model of linear $\delta^{34}S$-$^{87}Sr/^{86}Sr$ relationship (*15*) and overall similarity between Se and S isotope and elemental behavior during recycling—allows extrapolation

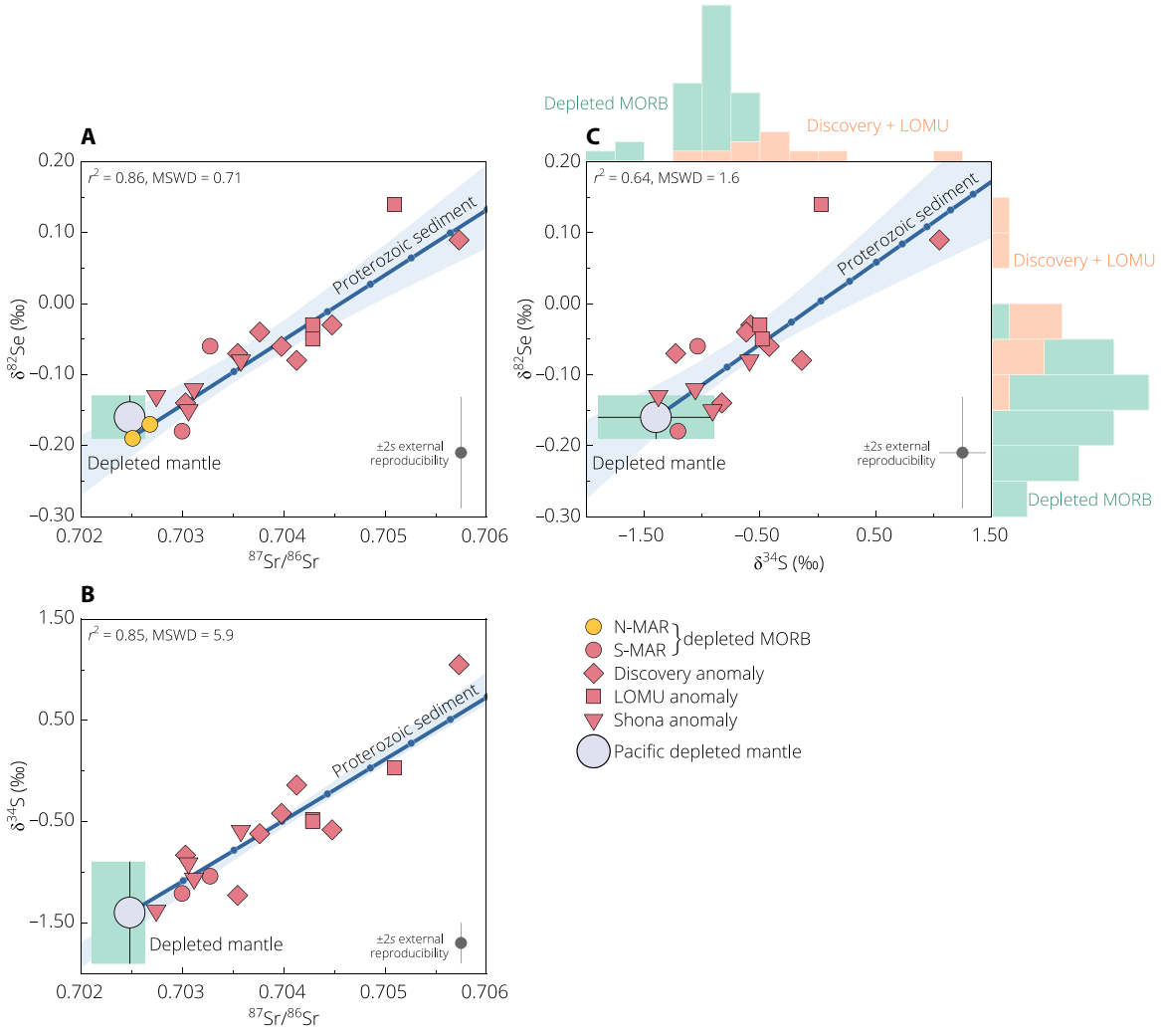

Fig. 3. δ^{82}Se, δ^{34}S, and ^{87}Sr/^{86}Sr data for MORB and the two-component mixing model. (**A** to **C**) The linear mixing lines are calculated using the most depleted MAR basalt or average Pacific depleted mantle (Table 1) as an anchor and the best-fit sediment end-member composition (δ^{82}Se and Se content; A and C) from a Yorkfit regression (Isoplot; section S5). External uncertainty on each isotopic value is considered for the regression, and shaded area indicates 95% CI error envelope. The S-Sr isotopic variation (B) is shown for comparison [δ^{34}S and S content of sediment in accordance with (*15*)]. Each tick mark on the mixing line denotes 0.1 weight % (wt %) sediment addition to the depleted mantle. See table S3 for model parameters. (C) also shows the frequency histogram of δ^{82}Se and δ^{34}S data (N = 41 and 44, respectively) across the MAR/PAR depleted MORB and Discovery plume-influenced MORB.

of the Se content and δ^{82}Se of recycled sediment using a simple linear mixing model (Figs. 4 and 5; see section S5 for details). An average Se content of 2.45 ± 0.71 μg/g (1*s*) is calculated for the recycled sediment using the well-constrained Se/Sr ratio of the depleted mantle and Sr content of recycled sediment (table S3). This value lies close to the +1*s* upper bound of the observed sediment average that is essentially identical for the 1- to 2-Ga age interval ($0.85^{+2.12}_{-0.61}$ μg/g, 1*s*) and the entire Proterozoic ($0.56^{+2.27}_{-0.45}$ μg/g, 1*s*; Fig. 5B). This argues against a significant, if any, Se loss (or modification of Se/Sr ratio) and hence associated isotopic fractionation from bulk sedimentary lithologies during subduction in the mid-Proterozoic and large-scale recycling in the mantle, reminiscent of that suggested for S (*15*) (see section S5 for discussion of more lines of evidence). Extrapolation of the linear regression to a model composition of 1.5-Ga-old recycled sediment ^{87}Sr/^{86}Sr = 0.7203 (*15*, *22*, *24*, *27*) yields δ^{82}Se = +1.44 ± 0.39‰ (95% CI; Fig. 4B). This value, although not uncommon in mid-Proterozoic sediments, is similar to or heavier than the +1*s* upper bound of the observed average for the 1- to 2-Ga interval (+0.62 ± 0.50‰; 1*s*, N = 76) or the entire Proterozoic (+0.53 ± 1.13‰; 1*s*, N = 210) (table S3 and Figs. 4B and 5A). This is reassuringly consistent with recycled pelagic sediments from a redox-stratified ocean (*9*), where the subduction of oceanic plate was predominantly associated with deep-ocean sediments deposited on the abyssal seafloor beyond the continental slope settings [e.g., (*12*)]. These abyssal sediments would be characterized by the highest δ^{82}Se because of near-quantitative reduction of water-soluble Se oxyanions under anoxic conditions, following partial reduction under oxic/suboxic conditions at shallower water depth (section S1 and fig. S1).

We further assess the applicability and robustness of the simple linear mixing model for characterization of the recycled sediment reservoir. Considering that the amount of sediment added to the S-MAR mantle is small [up to ~1 weight % (wt %) in our model; see also (*15*, *24*)], the δ^{82}Se-^{87}Sr/^{86}Sr array within the MORB data range

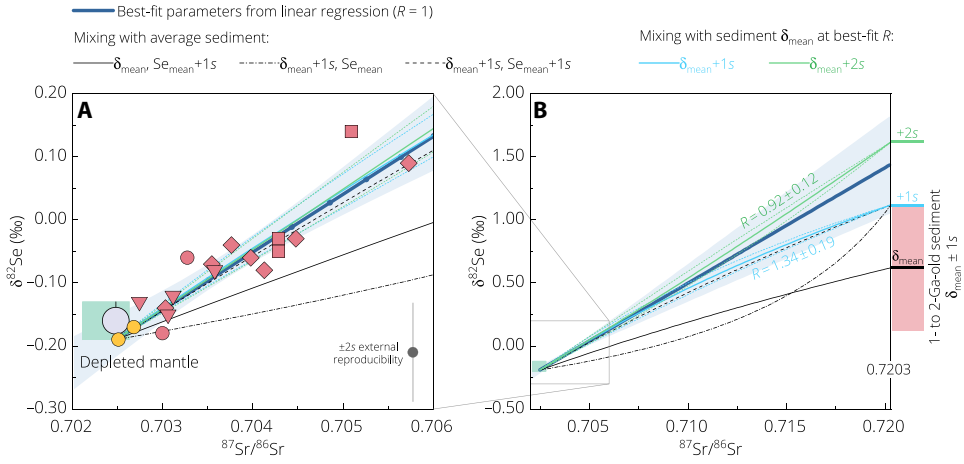

Fig. 4. Two-component mixing model with parameters from 1- to 2-Ga-old pelagic sediments. (**A**) displays segments of the mixing curves in (**B**) for the MORB data range. Symbols and the linear mixing array (±95% CI envelope) are the same as in Fig. 3. Black curves: Mixing trends using the well-constrained end-member parameters (δ^{82}Se, ^{87}Sr/^{86}Sr, and Se/Sr of depleted mantle; ^{87}Sr/^{86}Sr and Sr content of sediment) and observed sediment averages (δ^{82}Se and Se content) between mean and +1*s*. This indicates that the δ^{82}Se and Se content of recycled sediment in the S-MAR source must be both at least close to the +1*s* upper bound of observed sediment averages. Thin blue/green mixing trends are calculated at fixed upper bound δ^{82}Se of 1*s* and 2*s* above the mean; the curvature of the trend is controlled by $R = (Se/Sr)_{sediment}/(Se/Sr)_{mantle}$, which is calculated by error-weighted least-squares fitting of the mixing hyperbola (short-dashed lines correspond to ±95% CI on *R*). See table S3 and section S5 for model parameters and details.

might only represent a small segment of a hyperbolic mixing curve (Fig. 4B). Besides, Se content and δ^{82}Se of the sediment end member cannot be independently determined. The permissible range of these two variables, however, can be constrained. Our mixing models with the known range of 1- to 2-Ga-old sediment compositions (mean ± 1*s*) show that a realistic Se content and δ^{82}Se of recycled end member in the S-MAR source must be both at least comparable to the +1*s* upper bound of observed sediment averages (Fig. 4B). This result provides strong support for the idea (see above) that there was insignificant Se modification during sediment subduction and that recycled sediments dominantly reflect "abyssal" δ^{82}Se signature at the surface. Moreover, all the mixing arrays compatible with our MORB data and observed sediment averages (δ^{82}Se up to +2*s* upper bound) lie well within 95% CI range of the linear extrapolation (Fig. 4B), which, in turn, implies that the recycled sediment composition may be adequately estimated by a broadly linear mixing model. Accordingly, the possible δ^{82}Se range of recycled sediment calculated from the observed δ^{82}Se-^{87}Sr/^{86}Sr relationship at other reasonable recycling ages between 1 and 2 Ga (table S3) would also remain realistic for subducted sediments associated with prevalent deep-ocean anoxia (*9*) and hence does not alter our interpretation (Fig. 5A and section S5).

Mantle recycling record of atmospheric oxygenation

Subduction removed large portions of deep marine pyrites from the surface and thus transferred a significant Se reservoir into the deep-mantle source of our hot spots. This "lost-and-resurfaced" abyssal Se record complements the shallower marine pyrite record preserved on Earth's surface, which was used for reconstruction of the ocean-atmosphere redox evolution (Fig. 5, C and E) (*7*, *19*, *28*). Combining our result for the recycled sediment Se content (2.45 ± 0.71 μg/g; 1*s*) with the mean pyrite-bound S content of 1- to 2-Ga-old sediments [$1.1^{+1.4}_{-0.6}$ wt %; 1*s*, *N* = 85; (*10*, *29*)] and mean pyrite/matrix Se ratio of ~5.82 observed for sediments of all ages (*19*), we estimate a range of Se content between 13^{+4}_{-4} and 119^{+155}_{-74} μg/g (1*s*) for the recycled pyrite. This range depends on the relative contributions of pyrite and other matrices (organic matter, clay, and other silicates) to bulk Se budget in global black shales (section S5 and Fig. 5C) (*19*). A more realistic value probably tends toward our "lower estimate" because of the greater fraction of organic-bound Se in the mid-Proterozoic sediments compared with Phanerozoic sediments, where more abundant Se might be incorporated into pyrites after dissimilatory reduction of Se oxyanions in seawater (*20*). Invoking nonlinear mixing relationships between the depleted mantle and sediment would lead to different results for Se content of recycled pyrite, and its minimum possible range is calculated at fixed δ^{82}Se values of 1*s* and 2*s* above the observed mean of 1- to 2-Ga-old sediments (Fig. 4B and fig. S8; see section S5 for details). All these mixing models yield a "lower estimate" of recycled pyrite Se content that is comparable within error to the observed average of sedimentary pyrites formed during the 1- to 2-Ga interval (19^{+33}_{-12} μg/g) or entire Proterozoic [16^{+24}_{-10} μg/g, 1*s*; (*7*, *19*, *28*)] (table S3 and Fig. 5C and fig. S8E).

The notable similarity between the recycled abyssal and surface pyrite Se signatures from different depositional/redox environments lends additional support to the representativeness of Se in surface pyrites, although shallower, for atmospheric oxygen modeling (Fig. 5, C and E) (*7*). In turn, within the framework of the Large *et al.* (*7*) model, our Se concentration estimates for the recycled, abyssal pyrite support the idea of high atmospheric oxygen levels over an extended time interval (~50 to 100 million years; see above) in the mid-Proterozoic [on average, ~30 to 60% present atmospheric level (PAL); Fig. 5E]. Such a high oxygen estimate in (*7*) contrasts with earlier suggestions ranging from <0.1% to >4% PAL (*30*–*34*), with the most widely accepted range of ~0.01 to 10% PAL (*8*) (Fig. 5E); note, however, that it still remains lower than the threshold values required to sustain a fully oxygenated abyssal ocean [~70 to 80% PAL; (*35*)], consistent with the well-established mid-Proterozoic

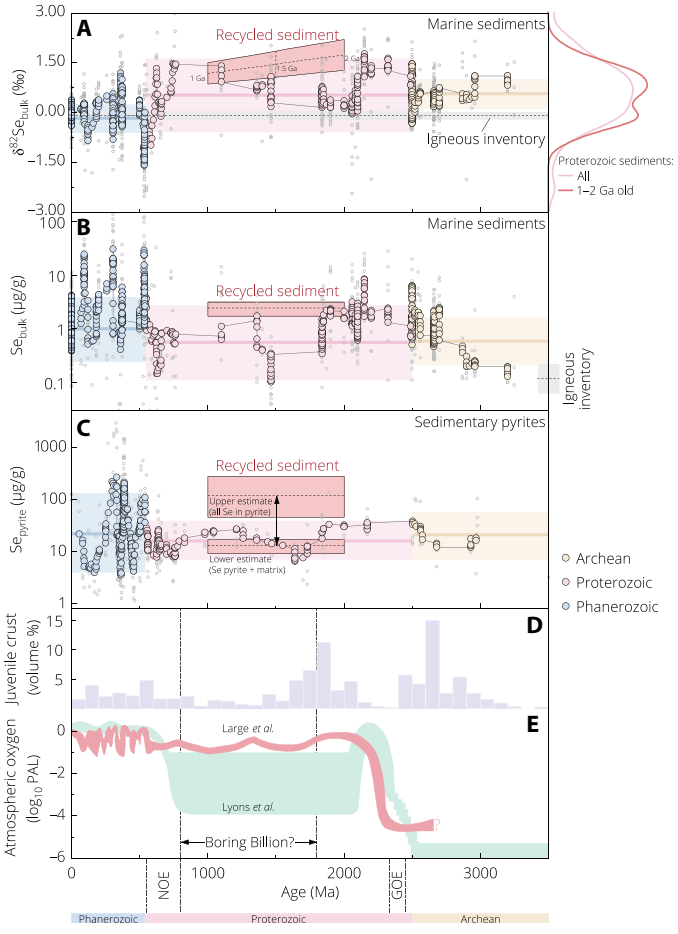

Fig. 5. Selenium geochemical record and atmospheric oxygenation through time. (**A** to **C**) Sediment Se record and our model results for ~1- to 2-Ga-old recycled sediment/pyrite (boxes; mean ± 95% CI for δ^{82}Se and 1*s* for Se content). Literature data are plotted as moving averages (large circles) of 11 individual sample data (small open circles) to highlight long-term evolution trends, with thick horizontal lines and shaded areas indicating mean ± 1*s* of each age interval. Igneous inventory: mean δ^{82}Se (−0.09 ± 0.12‰) and Se content ($0.120^{+0.107}_{-0.057}$ μg/g) of all mantle samples shown in Fig. 1. Right panel of (**A**): Gaussian kernel density estimates of sediment δ^{82}Se data for Proterozoic and 1- to 2-Ga interval (*N* = 210 and 76, respectively). (**D**) Temporal evolution of juvenile continental crust volume after (*47*). (**E**) Schematic illustration of atmospheric oxygen models of Large *et al.* (*7*) and Lyons *et al.* (*8*).

ocean redox structure [e.g., (*9*)] and the Se isotopic signature inferred for recycled sediments demonstrated above. Our compilation in Fig. 5 (A to E) illustrates first-order temporal trends in the Se systematics of marine sediments and sedimentary pyrites—together with the complementary deep-mantle abyssal record—in relation to major secular evolutions of the continental crust and atmospheric oxygen. These nuanced pictures seem to be inconsistent with the widely assumed static evolution of marine chemistry and low atmospheric oxygen across Earth's middle age [~0.8 to 1.8 Ga ago, also known as the "Boring Billion"; (*6*, *30*, *33*, *36*, *37*)] (Fig. 5E). Rather, as suggested by recently emerging models, it appears that Earth experienced a dynamic configuration of its surface and interior during this period toward a habitable world for the later emergence of complex life (*7*, *28*, *38*–*40*).

MATERIALS AND METHODS

Samples and chemical procedures

For this work, we selected a suite of well-characterized submarine glasses collected along the MAR (S- and N-MAR, *N* = 18; fig. S2). They include 14 enriched MORBs from the S-MAR interacting with the Discovery and Shona plumes and 2 depleted MORBs from each section of the MAR devoid of plume contribution. This is supplemented by the published δ^{82}Se data for PAR depleted MORBs (*N* = 27) (*21*). In addition, we report on δ^{82}Se measurements of three well-characterized granitoids from the Västervik area in Sweden, resembling materials derived from the mid-Proterozoic continental crust. See the Supplementary Materials for a detailed description of the geochemical background of the samples.

The sample digestion followed the method of (*41*). Samples were mixed with ^{74}Se-^{77}Se double spike and ^{125}Te spike and dissolved in an HF-HNO_3 mixture. This was followed by successive dissolutions and evaporations with HCl to eliminate the isobaric interference Ge. Samples were subsequently processed through anion and cation exchange chromatography for Se and Te purification. In the anion exchange column, Se was eluted following two different protocols, namely, "HCl chemistry" (*41*) and "HF chemistry" (this work). See the Supplementary Materials for full details.

Isotopic measurements

Concentrations of Se (when unknown) and Te were determined via the isotope dilution method on a Thermo Fisher Scientific iCAP-Qc inductively coupled plasma mass spectrometer (ICP-MS) linked with an ESI hydrideICP hydride generator (*41*). Selenium isotopes were analyzed on a Thermo Fisher Scientific NeptunePlus multicollector ICP-MS linked with an HGX-200 hydride generator (*42*). Before the final isotope measurements, sample solutions (1 ml of 2 N HCl) were monitored for residual Ge and further evaporated at 85°C in case of any detectable Ge (*41*). Procedural blanks (*N* = 4) were also checked at this stage, which yielded background signal intensities for all Se isotopes. Each sample analysis was bracketed by spiked NIST SRM 3149 standard (30 ng/ml), and Se isotope composition is reported relative to NIST SRM 3149 in ‰ units using δ^{82}Se notation

$$\delta^{82}\mathrm{Se}_{\mathrm{sample}} = (^{82}\mathrm{Se}/^{76}\mathrm{Se})_{\mathrm{sample}}/(^{82}\mathrm{Se}/^{76}\mathrm{Se})_{\mathrm{NIST\ SRM\ 3149}} - 1 \quad (1)$$

Most sample solutions contained ~10 to 35 ng of Se, which typically yields an internal error of <0.07‰ (95% CI based on 40 cycles of integration) for an individual measurement (tables S1 and S2). The interlaboratory standard MH-495 (30 ng/ml) included in each analytical session for quality control gives δ^{82}Se = −3.25 ± 0.07‰ (2*s*, *n* = 53), identical to literature data obtained under intermediate precision conditions (table S2). Together, these data allow us to estimate the 2*s* analytical precision of our method and yield an average δ^{82}Se = −3.25 ± 0.07‰ (2*s*, *n* = 200; table S2).

Several international rock standards processed together with the samples in this study are listed in table S1. The δ^{82}Se values of USGS (U.S. Geological Survey) rock standards BHVO-2 (*n* = 4), BCR-2 (*n* = 1), BIR-1a (*n* = 1), and W-2a (*n* = 2) are all in excellent agreement with the literature data. We additionally report on analyses of other certified rock standards JGb-1, MRG-1, and JA-3. The external reproducibility of our method for nonglass matrices is evaluated by pooling over all replicate analyses of rock standards (each >3 times) under intermediate precision conditions [e.g., (*43*)]

$$s_p = \sqrt{\frac{\sum_{i=1}^{N}\sum_{j=1}^{n_i}(\delta_{ij} - \overline{\delta}_i)^2}{\sum_{i=1}^{N}(n_i - 1)}} \quad (2)$$

where s_p is the pooled SD, N is the number of different samples, n_i is the number of replicate analyses of a sample, and δ_{ij} and $\overline{\delta}_i$ are the individual and average δ^{82}Se of a sample, respectively. This approach requires a homogeneity of variances across N groups of samples. This is validated by running a Bartlett's test over 52 analyses (51 digests) of five rock standards, which yields a test statistic of 0.78 and a p value of 0.94. Using Eq. 2, we obtained an external reproducibility of $2s_p = \pm 0.12‰$ for δ^{82}Se data of nonglass samples (table S1).

As for glass matrices, a recent study on PAR MORB reported higher reproducibility of $2s = 0.09‰$ on δ^{82}Se (*21*). To reevaluate our method reproducibility for glasses given the larger dataset here, we combined δ^{82}Se data from replicate analyses (>3 times) of three MAR glasses, which were randomly selected and processed via two different purification protocols, and the previously reported PAR MORB data (table S2). These groups of samples ($N = 4$, $n_i = 23$) passed the null hypothesis of the Bartlett's test with a test statistic of 1.57 and a p value of 0.67. Therefore, Eq. 2 can be used to calculate the pooled external reproducibility, which yields $2s_p = \pm 0.08‰$. This is similar to the analytical precision (±0.07‰) and is considerably lower than the reproducibility for nonglass basalts (±0.12‰), suggesting a significant Se isotope homogeneity in a glass matrix. Throughout the text and tables, the quoted uncertainty on a MORB δ^{82}Se value is 95% CI for the mean if $n_i > 3$, or the $2s_p$ external reproducibility of ±0.08‰ if $n_i \leq 3$. Replicate analyses of sample digests (MORBs and rock standards) that were randomly processed by the different purification chemistry in the anion column (i.e., HCl chemistry and HF chemistry) yield identical results within error (tables S1 and S2), further attesting to the robustness of our analytical procedure.

SUPPLEMENTARY MATERIALS

Supplementary material for this article is available at http://advances.sciencemag.org/cgi/content/full/6/39/eabb6179/DC1

REFERENCES AND NOTES

1. I. H. Campbell, C. M. Allen, Formation of supercontinents linked to increases in atmospheric oxygen. *Nat. Geosci.* **1**, 554–558 (2008).
2. C. B. Keller, B. Schoene, Statistical geochemistry reveals disruption in secular lithospheric evolution about 2.5 Gyr ago. *Nature* **485**, 490–493 (2012).
3. L. R. Kump, M. E. Barley, Increased subaerial volcanism and the rise of atmospheric oxygen 2.5 billion years ago. *Nature* **448**, 1033–1036 (2007).
4. C.-T. A. Lee, L. Y. Yeung, N. R. McKenzie, Y. Yokoyama, K. Ozaki, A. Lenardic, Two-step rise of atmospheric oxygen linked to the growth of continents. *Nat. Geosci.* **9**, 417–424 (2016).
5. M. A. Smit, K. Mezger, Earth's early O_2 cycle suppressed by primitive continents. *Nat. Geosci.* **10**, 788–792 (2017).
6. H. D. Holland, The oxygenation of the atmosphere and oceans. *Philos. Trans. R. Soc. Lond. B Biol. Sci.* **361**, 903–915 (2006).
7. R. R. Large, I. Mukherjee, D. Gregory, J. Steadman, R. Corkrey, L. V. Danyushevsky, Atmosphere oxygen cycling through the Proterozoic and Phanerozoic. *Miner. Deposita* **54**, 485–506 (2019).
8. T. W. Lyons, C. T. Reinhard, N. J. Planavsky, The rise of oxygen in Earth's early ocean and atmosphere. *Nature* **506**, 307–315 (2014).
9. S. W. Poulton, D. E. Canfield, Ferruginous conditions: A dominant feature of the ocean through Earth's history. *Elements* **7**, 107–112 (2011).
10. C. Scott, T. W. Lyons, A. Bekker, Y. Shen, S. W. Poulton, X. Chu, A. D. Anbar, Tracing the stepwise oxygenation of the Proterozoic ocean. *Nature* **452**, 456–459 (2008).
11. E. A. Sperling, C. J. Wolock, A. S. Morgan, B. C. Gill, M. Kunzmann, G. P. Halverson, F. A. Macdonald, A. H. Knoll, D. T. Johnston, Statistical analysis of iron geochemical data suggests limited late Proterozoic oxygenation. *Nature* **523**, 451–454 (2015).
12. P. J. Patchett, W. M. White, H. Feldmann, S. Kielinczuk, A. W. Hofmann, Hafnium/rare earth element fractionation in the sedimentary system and crustal recycling into the Earth's mantle. *Earth Planet. Sci. Lett.* **69**, 365–378 (1984).
13. M. B. Andersen, T. Elliott, H. Freymuth, K. W. Sims, Y. Niu, K. A. Kelley, The terrestrial uranium isotope cycle. *Nature* **517**, 356–359 (2015).
14. R. A. Cabral, M. G. Jackson, E. F. Rose-Koga, K. T. Koga, M. J. Whitehouse, M. A. Antonelli, J. Farquhar, J. M. Day, E. H. Hauri, Anomalous sulphur isotopes in plume lavas reveal deep mantle storage of Archaean crust. *Nature* **496**, 490–493 (2013).
15. J. Labidi, P. Cartigny, M. Moreira, Non-chondritic sulphur isotope composition of the terrestrial mantle. *Nature* **501**, 208–211 (2013).
16. H. Liu, R. E. Zartman, T. R. Ireland, W. D. Sun, Global atmospheric oxygen variations recorded by Th/U systematics of igneous rocks. *Proc. Natl. Acad. Sci. U.S.A.* **116**, 18854–18859 (2019).
17. D. A. Stolper, C. E. Bucholz, Neoproterozoic to early Phanerozoic rise in island arc redox state due to deep ocean oxygenation and increased marine sulfate levels. *PNAS* **116**, 8746–8755 (2019).
18. T. M. Johnson, T. D. Bullen, Mass-dependent fractionation of selenium and chromium isotopes in low-temperature environments. *Rev. Mineral. Geochem.* **55**, 289–317 (2004).
19. R. R. Large, J. A. Halpin, L. V. Danyushevsky, V. V. Maslennikov, S. W. Bull, J. A. Long, D. D. Gregory, E. Lounejeva, T. W. Lyons, P. J. Sack, P. J. McGoldrick, C. R. Calver, Trace element content of sedimentary pyrite as a new proxy for deep-time ocean–atmosphere evolution. *Earth Planet. Sci. Lett.* **389**, 209–220 (2014).
20. E. E. Stüeken, R. Buick, A. Bekker, D. Catling, J. Foriel, B. M. Guy, L. C. Kah, H. G. Machel, I. P. Montanez, S. W. Poulton, The evolution of the global selenium cycle: Secular trends in Se isotopes and abundances. *Geochim. Cosmochim. Acta* **162**, 109–125 (2015).
21. A. Yierpan, S. König, J. Labidi, R. Schoenberg, Selenium isotope and S-Se-Te elemental systematics along the Pacific-Antarctic ridge: Role of mantle processes. *Geochim. Cosmochim. Acta* **249**, 199–224 (2019).
22. M. Andres, J. Blichert-Toft, J.-G. Schilling, Hafnium isotopes in basalts from the southern Mid-Atlantic Ridge from 40°S to 55°S: Discovery and Shona plume-ridge interactions and the role of recycled sediments. *Geochem. Geophys. Geosyst.* **3**, 1–25 (2002).
23. J. Douglass, J.-G. Schilling, D. Fontignie, Plume-ridge interactions of the Discovery and Shona mantle plumes with the southern Mid-Atlantic Ridge (40°-55°S). *J. Geophys. Res.* **104**, 2941–2962 (1999).
24. P. J. le Roux, A. P. le Roex, J.-G. Schilling, N. Shimizu, W. W. Perkins, N. J. G. Pearce, Mantle heterogeneity beneath the southern Mid-Atlantic Ridge: Trace element evidence for contamination of ambient asthenospheric mantle. *Earth Planet. Sci. Lett.* **203**, 479–498 (2002).
25. E. M. Syracuse, G. A. Abers, Global compilation of variations in slab depth beneath arc volcanoes and implications. *Geochem. Geophys. Geosyst.* **7**, 10.1029/2005GC001045, (2006).
26. Z. Zhang, A. von der Handt, M. M. Hirschmann, An experimental study of Fe–Ni exchange between sulfide melt and olivine at upper mantle conditions: Implications for mantle sulfide compositions and phase equilibria. *Contrib. Mineral. Petrol.* **173**, 19 (2018).
27. M. Rehkämper, A. W. Hofmann, Recycled ocean crust and sediment in Indian Ocean MORB. *Earth Planet. Sci. Lett.* **147**, 93–106 (1997).
28. I. Mukherjee, R. R. Large, R. Corkrey, L. V. Danyushevsky, The Boring Billion, a slingshot for complex life on Earth. *Sci. Rep.* **8**, 4432 (2018).
29. S. W. Poulton, P. W. Fralick, D. E. Canfield, The transition to a sulphidic ocean approximately 1.84 billion years ago. *Nature* **431**, 173–177 (2004).
30. E. J. Bellefroid, A. V. S. Hood, P. F. Hoffman, M. D. Thomas, C. T. Reinhard, N. J. Planavsky, Constraints on Paleoproterozoic atmospheric oxygen levels. *Proc. Natl. Acad. Sci. U.S.A.* **115**, 8104–8109 (2018).
31. D. E. Canfield, S. Zhang, A. B. Frank, X. Wang, H. Wang, J. Su, Y. Ye, R. Frei, Highly fractionated chromium isotopes in Mesoproterozoic-aged shales and atmospheric oxygen. *Nat. Commun.* **9**, 2871 (2018).
32. G. J. Gilleaudeau, R. Frei, A. J. Kaufman, L. C. Kah, K. Azmy, J. K. Bartley, P. Chernyavskiy, A. H. Knoll, Oxygenation of the mid-Proterozoic atmosphere: Clues from chromium isotopes in carbonates. *Geochem Perspect Let* **2**, 178–187 (2016).
33. N. J. Planavsky, C. T. Reinhard, X. Wang, D. Thomson, P. McGoldrick, R. H. Rainbird, T. Johnson, W. W. Fischer, T. W. Lyons, Earth history. Low mid-Proterozoic atmospheric oxygen levels and the delayed rise of animals. *Science* **346**, 635–638 (2014).
34. S. Zhang, X. Wang, H. Wang, C. J. Bjerrum, E. U. Hammarlund, M. M. Costa, J. N. Connelly, B. Zhang, J. Su, D. E. Canfield, Sufficient oxygen for animal respiration 1,400 million years ago. *Proc. Natl. Acad. Sci. U.S.A.* **113**, 1731–1736 (2016).
35. L. J. Alcott, B. J. W. Mills, S. W. Poulton, Stepwise Earth oxygenation is an inherent property of global biogeochemical cycling. *Science* **366**, 1333–1337 (2019).
36. M. D. Brasier, J. F. Lindsay, A billion years of environmental stability and the emergence of eukaryotes: New data from northern Australia. *Geology* **26**, 555–558 (1998).
37. P. A. Cawood, C. J. Hawkesworth, Earth's middle age. *Geology* **42**, 503–506 (2014).
38. C. Doglioni, J. Pignatti, M. Coleman, Why did life develop on the surface of the Earth in the Cambrian? *Geosci. Front.* **7**, 865–873 (2016).
39. W. B. Hamilton, Toward a myth-free geodynamic history of Earth and its neighbors. *Earth Sci. Rev.* **198**, 102905 (2019).

40. I. Mukherjee, R. R. Large, Co-evolution of trace elements and life in Precambrian oceans: The pyrite edition. *Geology*, (2020).
41. A. Yierpan, S. König, J. Labidi, T. Kurzawa, M. G. Babechuk, R. Schoenberg, Chemical sample processing for combined selenium isotope and selenium-tellurium elemental investigation of the Earth's igneous reservoirs. *Geochem. Geophys. Geosyst.* **19**, 516–533 (2018).
42. T. Kurzawa, S. König, J. Labidi, A. Yierpan, R. Schoenberg, A method for Se isotope analysis of low ng-level geological samples via double spike and hydride generation MC-ICP-MS. *Chem. Geol.* **466**, 219–228 (2017).
43. R. C. Hin, C. D. Coath, P. J. Carter, F. Nimmo, Y. J. Lai, P. A. E. Pogge von Strandmann, M. Willbold, Z. M. Leinhardt, M. J. Walter, T. Elliott, Magnesium isotope evidence that accretional vapour loss shapes planetary compositions. *Nature* **549**, 511–515 (2017).
44. A. Stracke, Earth's heterogeneous mantle: A product of convection-driven interaction between crust and mantle. *Chem. Geol.* **330-331**, 274–299 (2012).
45. A. Agranier, J. Blichert-Toft, D. Graham, V. Debaille, P. Schiano, F. Albarede, The spectra of isotopic heterogeneities along the mid-Atlantic Ridge. *Earth Planet. Sci. Lett.* **238**, 96–109 (2005).
46. J. Labidi, P. Cartigny, C. Hamelin, M. Moreira, L. Dosso, Sulfur isotope budget (^{32}S, ^{33}S, ^{34}S and ^{36}S) in Pacific–Antarctic ridge basalts: A record of mantle source heterogeneity and hydrothermal sulfide assimilation. *Geochim. Cosmochim. Acta* **133**, 47–67 (2014).
47. D. I. Groves, R. M. Vielreicher, R. J. Goldfarb, K. C. Condie, Controls on the heterogeneous distribution of mineral deposits through time. *Geol Soc Spec Publ* **248**, 71–101 (2005).
48. J.-I. Kimura, J. B. Gill, P. E. van Keken, H. Kawabata, S. Skora, Origin of geochemical mantle components: Role of spreading ridges and thermal evolution of mantle. *Geochem. Geophys. Geosyst.* **18**, 697–734 (2017).
49. J. Douglass, J.-G. Schilling, R. H. Kingsley, Influence of the discovery and Shona mantle plumes on the southern Mid-Atlantic ridge: Rare earth evidence. *Geophys. Res. Lett.* **22**, 2893–2896 (1995).
50. J.-G. Schilling, M. Zajac, R. Evans, T. Johnston, W. White, J. D. Devine, R. Kingsley, Petrologic and geochemical variations along the Mid-Atlantic ridge from 29 degrees N to 73 degrees N. *Am. J. Sci.* **283**, 510–586 (1983).
51. W. M. White, J.-G. Schilling, The nature and origin of geochemical variation in Mid-Atlantic Ridge basalts from the Central North Atlantic. *Geochim. Cosmochim. Acta* **42**, 1501–1516 (1978).
52. J. Blichert-Toft, A. Agranier, M. Andres, R. Kingsley, J.-G. Schilling, F. Albarède, Geochemical segmentation of the Mid-Atlantic Ridge north of Iceland and ridge-hot spot interaction in the North Atlantic. *Geochem. Geophys. Geosyst.* **6**, (2005).
53. M. Moreira, T. Staudacher, P. Sarda, J.-G. Schilling, C. J. Allègre, A primitive plume neon component in MORB: The Shona ridge-anomaly, South Atlantic (51–52°S). *Earth Planet. Sci. Lett.* **133**, 367–377 (1995).
54. P. Sarda, M. Moreira, T. Staudacher, J.-G. Schilling, C. J. Allègre, Rare gas systematics on the southernmost Mid-Atlantic Ridge: Constraints on the lower mantle and the Dupal source. *J. Geophys. Res.* **105**, 5973–5996 (2000).
55. K. A. Kelley, R. Kingsley, J.-G. Schilling, Composition of plume-influenced mid-ocean ridge lavas and glasses from the Mid-Atlantic Ridge, East Pacific Rise, Galápagos Spreading Center, and Gulf of Aden. *Geochem. Geophys. Geosyst.* **14**, 223–242 (2013).
56. P. J. le Roux, A. le Roex, J.-G. Schilling, Crystallization processes beneath the southern Mid-Atlantic Ridge (40–55°S), evidence for high-pressure initiation of crystallization. *Contrib. Mineral. Petrol.* **142**, 582–602 (2002).
57. P. J. le Roux, A. le Roex, J.-G. Schilling, MORB melting processes beneath the southern Mid-Atlantic Ridge (40–55°S): A role for mantle plume-derived pyroxenite. *Contrib. Mineral. Petrol.* **144**, 206–229 (2002b).
58. I. C. Kleinhanns, M. J. Whitehouse, N. Nolte, W. Baero, F. Wilsky, B. T. Hansen, R. Schoenberg, Mode and timing of granitoid magmatism in the Västervik area (SE Sweden, Baltic Shield): Sr–Nd isotope and SIMS U–Pb age constraints. *Lithos* **212-215**, 321–337 (2015).
59. N. Nolte, I. C. Kleinhanns, W. Baero, B. T. Hansen, Petrography and whole-rock geochemical characteristics of Västervik granitoids to syenitoids, southeast Sweden: Constraints on petrogenesis and tectonic setting at the southern margin of the Svecofennian domain. *Gff* **133**, 173–196 (2011).
60. T. Kurzawa, S. König, J. C. Alt, A. Yierpan, R. Schoenberg, The role of subduction recycling on the selenium isotope signature of the mantle: Constraints from Mariana arc lavas. *Chem. Geol.* **513**, 239–249 (2019).
61. M. I. Varas-Reus, S. König, A. Yierpan, J. P. Lorand, R. Schoenberg, Selenium isotopes as tracers of a late volatile contribution to Earth from the outer Solar System. *Nat. Geosci.* **12**, 779–782 (2019).
62. O. Rouxel, A. Galy, H. Elderfield, Germanium isotopic variations in igneous rocks and marine sediments. *Geochim. Cosmochim. Acta* **70**, 3387–3400 (2006).
63. T. Yokoyama, A. Makishima, E. Nakamura, Evaluation of the coprecipitation of incompatible trace elements with fluoride during silicate rock dissolution by acid digestion. *Chem. Geol.* **157**, 175–187 (1999).
64. G. A. Cutter, L. S. Cutter, Sources and cycling of selenium in the western and equatorial Atlantic Ocean. *Deep-Sea Res. Pt Ii* **48**, 2917–2931 (2001).
65. E. E. Stüeken, Selenium isotopes as a biogeochemical proxy in deep time. *Rev. Mineral. Geochem.* **82**, 657–682 (2017).
66. E. E. Stüeken, R. Buick, A. D. Anbar, Selenium isotopes support free O2 in the latest Archean. *Geology* **43**, 259–262 (2015).
67. S. König, B. Eickmann, T. Zack, A. Yierpan, M. Wille, H. Taubald, R. Schoenberg, Redox induced sulfur-selenium isotope decoupling recorded in pyrite. *Geochim. Cosmochim. Acta* **244**, 24–39 (2019).
68. K. Mitchell, P. R. D. Mason, P. Van Cappellen, T. M. Johnson, B. C. Gill, J. D. Owens, J. Diaz, E. D. Ingall, G. J. Reichart, T. W. Lyons, Selenium as paleo-oceanographic proxy: A first assessment. *Geochim. Cosmochim. Acta* **89**, 302–317 (2012).
69. M. A. Kipp, T. J. Algeo, E. E. Stüeken, R. Buick, Basinal hydrographic and redox controls on selenium enrichment and isotopic composition in Paleozoic black shales. *Geochim. Cosmochim. Acta* , (2019).
70. M. A. Kipp, E. E. Stueken, A. Bekker, R. Buick, Selenium isotopes record extensive marine suboxia during the Great Oxidation Event. *Proc. Natl. Acad. Sci. U.S.A.* **114**, 875–880 (2017).
71. M. C. Koehler, R. Buick, M. A. Kipp, E. E. Stueken, J. Zaloumis, Transient surface ocean oxygenation recorded in the ~2.66-Ga Jeerinah Formation, Australia. *Proc. Natl. Acad. Sci. U.S.A.* **115**, 7711–7716 (2018).
72. K. Mitchell, S. Z. Mansoor, P. R. D. Mason, T. M. Johnson, P. Van Cappellen, Geological evolution of the marine selenium cycle: Insights from the bulk shale δ 82/76 Se record and isotope mass balance modeling. *Earth Planet. Sci. Lett.* **441**, 178–187 (2016).
73. P. A. E. Pogge von Strandmann, E. E. Stüeken, T. Elliott, S. W. Poulton, C. M. Dehler, D. E. Canfield, D. C. Catling, Selenium isotope evidence for progressive oxidation of the Neoproterozoic biosphere. *Nat. Commun.* **6**, (2015).
74. A. J. T. Shore, Selenium geochemistry and isotopic composition of sediments from the Cariaco Basin and the Bermuda Rise: A comparison between a restricted basin and the open ocean over the last 500 ka. Ph.D. thesis, University of Leicester, Leicester, UK (2010).
75. H. J. Wen, J. Carignan, X. L. Chu, H. F. Fan, C. Cloquet, J. Huang, Y. X. Zhang, H. J. Chang, Selenium isotopes trace anoxic and ferruginous seawater conditions in the Early Cambrian. *Chem. Geol.* **390**, 164–172 (2014).
76. M. Lissner, S. König, A. Luguet, P. J. le Roux, S. Schuth, A. Heuser, A. P. le Roex, Selenium and tellurium systematics in MORBs from the southern Mid-Atlantic Ridge (47–50°S). *Geochim. Cosmochim. Acta* **144**, 379–402 (2014).
77. J. M. Brenan, Se–Te fractionation by sulfide–silicate melt partitioning: Implications for the composition of mantle-derived magmas and their melting residues. *Earth Planet. Sci. Lett.* **422**, 45–57 (2015).
78. F. E. Jenner, E. H. Hauri, E. S. Bullock, S. König, R. J. Arculus, J. A. Mavrogenes, N. Mikkelson, C. Goddard, The competing effects of sulfide saturation versus degassing on the behavior of the chalcophile elements during the differentiation of hydrous melts. *Geochem. Geophys. Geosyst.* **16**, 1490–1507 (2015).
79. J. Labidi, P. Cartigny, Negligible sulfur isotope fractionation during partial melting: Evidence from Garrett transform fault basalts, implications for the late-veneer and the hadean matte. *Earth Planet. Sci. Lett.* **451**, 196–207 (2016).
80. K. R. Ludwig, Isoplot 3.71. Berkeley Geochronology Centre (2008).
81. C. J. Allègre, D. L. Turcotte, Implications of a two-component marble-cake mantle. *Nature* **323**, 123–127 (1986).
82. C. Hamelin, L. Dosso, B. B. Hanan, M. Moreira, A. P. Kositsky, M. Y. Thomas, Geochemical portray of the Pacific Ridge: New isotopic data and statistical techniques. *Earth Planet. Sci. Lett.* **302**, 154–162 (2011).
83. O. Rouxel, J. Ludden, J. Carignan, L. Marin, Y. Fouquet, Natural variations of Se isotopic composition determined by hydride generation multiple collector inductively coupled plasma mass spectrometry. *Geochim. Cosmochim. Acta* **66**, 3191–3199 (2002).
84. J. Labidi, S. König, T. Kurzawa, A. Yierpan, R. Schoenberg, The selenium isotopic variations in chondrites are mass-dependent; Implications for sulfide formation in the early solar system. *Earth Planet Sci. Lett.* **481**, 212–222 (2018).
85. W. F. Mcdonough, S.-S. Sun, The Composition of the Earth. *Chem. Geol.* **120**, 223–253 (1995).
86. Z. Wang, H. Becker, Ratios of S, Se and Te in the silicate Earth require a volatile-rich late veneer. *Nature* **499**, 328–331 (2013).
87. H. Palme, H. S. C. O'Neill, in *Treatise on Geochemistry (Second Edition),* H. D. Holland, K. K. Turekian, Eds. (Elsevier, Oxford, 2014), pp. 1–39.
88. V. J. M. Salters, A. Stracke, Composition of the depleted mantle. *Geochem. Geophys. Geosyst.* **5**, Q05B07 (2004).
89. T. Plank, in *Treatise on Geochemistry,* H. D. Holland, K. K. Turekian, Eds. (Elsevier, Oxford, 2014), pp. 607–629.
90. C. T. A. Lee, M. Erdman, W. B. Yang, L. Ingram, E. J. Chin, D. J. DePaolo, Sulfur isotopic compositions of deep arc cumulates. *Earth Planet. Sci. Lett.* **500**, 76–85 (2018).
91. R. L. Rudnick, S. Gao, in *Treatise on Geochemistry,* H. D. Holland, K. K. Turekian, Eds. (Pergamon, Oxford, 2003), pp. 1–64.

92. F. E. Jenner, Cumulate causes for the low contents of sulfide-loving elements in the continental crust. *Nat. Geosci.* **10**, 524–529 (2017).
93. W. Xu, J.-M. Zhu, T. M. Johnson, X. Wang, Z.-Q. Lin, D. Tan, H. Qin, Selenium isotope fractionation during adsorption by Fe, Mn and Al oxides. *Geochim. Cosmochim. Acta* **272**, 121–136 (2020).
94. G. H. Floor, G. Román-Ross, Selenium in volcanic environments: A review. *Appl. Geochem.* **27**, 517–531 (2012).
95. A. Gale, C. A. Dalton, C. H. Langmuir, Y. Su, J.-G. Schilling, The mean composition of ocean ridge basalts. *Geochem. Geophys. Geosyst.* **14**, 489–518 (2013).
96. A. Stracke, M. Bizimis, V. J. M. Salters, Recycling oceanic crust: Quantitative constraints. *Geochem. Geophys. Geosyst.* **4**, (2003).

Acknowledgments: We would like to thank I. Kleinhanns for providing the three Västervik granitoid samples and K. A. Kelley for the two N-MAR samples. We are grateful to E. Reitter and B. Steinhilber for their dedicated analytical support, and M. Wille, F. Ossa Ossa, and B. Eickmann for continued discussion. We also thank three anonymous reviewers for thorough and constructive reviews, and C.-T. A. Lee for editorial handling. **Funding:** This work was financially supported by the European Research Council (ERC) Starting Grant O2RIGIN (636808) to S.K. **Author contributions:** S.K. conceived and directed the research. A.Y. conducted the measurements, interpreted the data, and wrote the paper, with input from S.K., J.L., and R.S. **Competing interests:** The authors declare that they have no competing interests. **Data and materials availability:** All data needed to evaluate the conclusions in the paper are present in the paper and/or the Supplementary Materials. Additional data related to this paper may be requested from the corresponding authors.

Submitted 6 March 2020
Accepted 3 August 2020
Published 23 September 2020
10.1126/sciadv.abb6179

Citation: A. Yierpan, S. König, J. Labidi, R. Schoenberg, Recycled selenium in hot spot–influenced lavas records ocean-atmosphere oxygenation. *Sci. Adv.* **6**, eabb6179 (2020).

Science Advances

Recycled selenium in hot spot–influenced lavas records ocean-atmosphere oxygenation

Aierken Yierpan, Stephan König, Jabrane Labidi and Ronny Schoenberg

Sci Adv **6** (39), eabb6179.
DOI: 10.1126/sciadv.abb6179